Xia et al. Nanoscale Research Letters (2018) 13:148
https://doi.org/10.1186/s11671-018-2558-6

Nanoscale Research Letters

NANO EXPRESS Open Access

# Fabrication and Photocatalytic Property of Novel $SrTiO_3/Bi_5O_7I$ Nanocomposites

Yongmei Xia[1,4], Zuming He[2,3*], Jiangbin Su[2,3], Ya Liu[4] and Bin Tang[2,3*]

## Abstract

The novel $SrTiO_3/Bi_5O_7I$ nanocomposites were successfully fabricated by a thermal decomposition approach. The as-prepared samples were characterized by XRD, XPS, SEM, EDS, FTIR, DRS and PL spectra. The results show that the $SrTiO_3/Bi_5O_7I$ nanocomposites are composed of perovskite $SrTiO_3$ nanoparticles and tetragonal $Bi_5O_7I$ nanorods. The $SrTiO_3/Bi_5O_7I$ nanocomposites exhibit an excellent photocatalytic performance for the degradation of RhB solution under simulated solar light irradiation, which is superior to that of pristine $Bi_5O_7I$ and $SrTiO_3$. In particular, the 30 wt% $SrTiO_3/Bi_5O_7I$ nanocomposite is found as the optimal composites, over which the dye degradation reaches 89.6% for 150 min of photocatalysis. The photocatalytic degradation rate of the 30 wt% $SrTiO_3/Bi_5O_7I$ nanocomposite is found to be 3.97 times and 12.5 times higher than that of bare $Bi_5O_7I$ and $SrTiO_3$, respectively. The reactive species trapping experiments suggest that $\cdot O_2^-$ and holes are the main active species responsible for the RhB degradation. In addition, the PL spectra elucidate the effective separation of photoinduced electron-hole pairs. Further, the possible photocatalytic mechanism of the $SrTiO_3/Bi_5O_7I$ nanocomposites is also elucidated based on the experimental evidences.

**Keywords:** $SrTiO_3$, $Bi_5O_7I$, Nanocomposite, Photocatalytic, Mechanism

## Background

Dyes from textile or dyestuff industries have aroused much concern for the impact on the quality of water resources and the toxic and carcinogenic degradation products [1]. Therefore, more competent treatment techniques are needed for the complete elimination of dyes form wastewater. Several conventional methods involving physical, chemical, and biological methods have been applied for dye remediation from wastewater [2]. These methods can remove dyes from wastewater, but they are often expensive, inefficient, and produce secondary waste products [3, 4]. Among various dye wastewater treatment technologies, semiconductor-based photocatalysis has received a great interest and attracted worldwide attention [5–7]. This is because it utilizes solar energy for the decomposition of dye pollutants, whose source of energy is abundant, inexhaustible, non-polluting, and free [8, 9]. At present, $TiO_2$ is the most widely used semiconductor photocatalyst due to its high photoactivity, low cost, chemical and photochemical stability, non-toxicity, and environmentally friendly features. However, it showed a very low photocatalytic activity under visible light irradiation due to its wide band gap of 3.2 eV and the rapid recombination of photogenerated carriers [10]. To effectively solve the above mentioned problems, much work has been devoted to the surface modification or the combination of semiconductor photocatalysts [11]. Nevertheless, the development of novel and highly efficient photocatalysts still remains a major challenge [12].

$Bi_5O_7I$ is a newly found p-type semiconductor, which shows a relatively more positive valence band (VB) level than other bismuth oxyiodides by providing more photoexcited holes and subsequently facilitates the separation of photogenerated carriers [13]. Therefore, the $Bi_5O_7I$ photocatalyst exhibits a high activity for the photodegradation of Rhodamine B (RhB) in water and acetaldehyde under visible light irradiation [14]. Unfortunately, the practical application of $Bi_5O_7I$ photocatalyst in the environmental decontamination is still limited, which is attributed to its low transfer efficiency caused by the recombination of photogenerated electrons and holes [15]. For the purpose of further improving the photoactivity of $Bi_5O_7I$, many attempts have been carried out such as doping with metals

* Correspondence: hezuming432928@126.com; btang@cczu.edu.cn
[2]Huaide College, Changzhou University, Jingjiang 214500, China
Full list of author information is available at the end of the article

or non-metals [16], or coupling with other semiconductors. For instance, Huang et al. synthesized g-$C_3N_4$/$Bi_5O_7I$ heterojunction via a co-crystallization method, and the composite exhibited a degradation rate 2.9 times higher than that of pure $Bi_5O_7I$ [17]; Cheng et al. fabricated $Bi_5O_7I$/$Bi_2O_3$ composite via chemical etching method, which showed a high photocatalytic activity in decomposition of malachite green [18]; Hu et al. reported that a composite comprising n-type $Sr_2TiO_4$ and p-type $Bi_5O_7I$ showed an enhanced photoactivity because of the inhibition of electron-hole recombination [19]; Cui et al. fabricated AgI/$Bi_5O_7I$ hybrid via a simple one-step ionic reaction, and the AgI/$Bi_5O_7I$ composite enhanced the photocatalytic activity [20], and so on. These results showed that $Bi_5O_7I$-based composites exhibited an enhanced photocatalytic performance under visible light irradiation. Therefore, we can fabricate $Bi_5O_7I$-based composites through coupling to another semiconductor with suitable conduction band (CB) and VB positions as a promising visible-light-driven photocatalyst. Among various candidates, strontium titanate ($SrTiO_3$) is an n-type semiconductor material, which has been extensively studied because of its many excellent properties, e.g., thermal stability, good heat resistance, corrosion, and resistance [21–23]. Pure $SrTiO_3$ only absorbs UV light due to its wide band gap of 3.1~3.4 eV [24]. Fortunately, the VB of $SrTiO_3$ is positioned between the CB and VB of $Bi_5O_7I$, while its CB is positioned above the CB of $Bi_5O_7I$. Considering the structural merits of $Bi_5O_7I$, combination of $SrTiO_3$ with $Bi_5O_7I$ to form the $SrTiO_3$/$Bi_5O_7I$ composite may be a viable and advisable way to realize the high photocatalytic activity.

In this work, a series of $SrTiO_3$/$Bi_5O_7I$ nanocomposite photocatalysts were first synthesized. Their crystal phase, microstructure, and optical properties were investigated by a series of techniques. The $SrTiO_3$/$Bi_5O_7I$ nanocomposites displayed an enhanced photocatalytic performance in the degradation of Rhodamine B (RhB) solution under simulated solar light irradiation. Further, the possible photocatalytic mechanism of the $SrTiO_3$/$Bi_5O_7I$ nanocomposites was also elucidated based on the experimental evidences.

## Methods

### Preparation of $SrTiO_3$/$Bi_5O_7I$ Composites

$SrTiO_3$ nanoparticles and $SrTiO_3$/BiOI composites were firstly synthesized via a sol-gel method as described in the literature [25, 26]. $SrTiO_3$/$Bi_5O_7I$ composites were then synthesized by a thermal decomposition route. All the chemical reagents were used directly for the experiments without any further purification. During the thermal decomposition, the as-prepared $SrTiO_3$/BiOI composites were placed into a tube furnace, and the heating program was set as follows: ramping at 5 °C $min^{-1}$ to 500 °C continuously and holding at 500 °C for 3 h. Then, the furnace was naturally cooled to room temperature to obtain 10 wt% $SrTiO_3$/$Bi_5O_7I$ nanocomposite. Other $SrTiO_3$/$Bi_5O_7I$ nanocomposite materials with different $SrTiO_3$ content were fabricated by the similar method.

### Sample Characterization

The crystal structures of the synthesized samples were characterized using X-ray diffraction (XRD) with Cu $K_\alpha$ radiation (D/max-2500, Rigaku). The morphology of the samples was investigated by an ultrahigh resolution field-emission scanning electron microscope (FE-SEM; SUAPR55, Germany Zeiss) with energy-disperse X-ray spectroscopy (EDS). The surface elemental component and the chemical state of the samples were analyzed by X-ray photoelectron spectroscopy (XPS; Axis Ultra DLD, Kratos Analytical, UK) with a monochromatized Al $K_\alpha$ X-ray source (hν = 1486.6 eV). The ultraviolet-visible (UV-vis) diffuse reflectance spectra (DRS) were obtained using a UV-vis spectrophotometer (UV-2450, Shimadzu). The functional groups on the surface of the samples were investigated in a Nicolet iS50 fourier-transform infrared spectroscopy (FTIR; Thermo Fisher Scientific, USA). The photoluminescence (PL) emission spectra were measured on a LH110911 steady-state fluorescence spectrometer.

### Photocatalytic Evaluation Studies

The photocatalytic activity of the materials was evaluated via the decomposition of RhB under simulated solar light (UV light) irradiation in a photoreaction apparatus. After 30 min adsorption in darkness, the adsorption-desorption is at an equilibrium between photocatalyst and RhB molecules. A 500 W xenon lamp was used as a simulated solar light (UV lamp) source. One hundred milligrams of photocatalyst was completely dispersed in 100 mL RhB solution (20 mg/L). During each photocatalytic experiment, 3 mL of the suspension was pipet out every 30 min and centrifuged to remove catalyst particles. The concentration of the RhB was measured using UV-vis spectrophotometer.

## Results and Discussion

### XRD Analysis

The powder XRD patterns provide the crystal structure and phase information of the synthesized samples, as shown in Fig. 1. The $SrTiO_3$ sample is highly crystallized with a perovskite structure (JCPDS no. 35-0734). The diffraction peaks at the 2$\theta$ values of 22.75°, 32.39°, 39.95°, 46.47°, 52.34°, 57.78°, 67.82°, and 77.18° can be indexed to (100), (110), (111), (200), (210), (211), (220), and (310) crystal planes, respectively [27]. No other specific diffraction peak is detected. From the XRD pattern of pure $Bi_5O_7I$, it can be seen that the main diffraction peaks at 7.71°, 13.31°, 15.38°, 23.19°, 28.08°, 31.09°, 33.43°, 46.28°, 47.69°, 53.45°, 56.51°, and 58.02° are conforming to the (001), (201), (002),

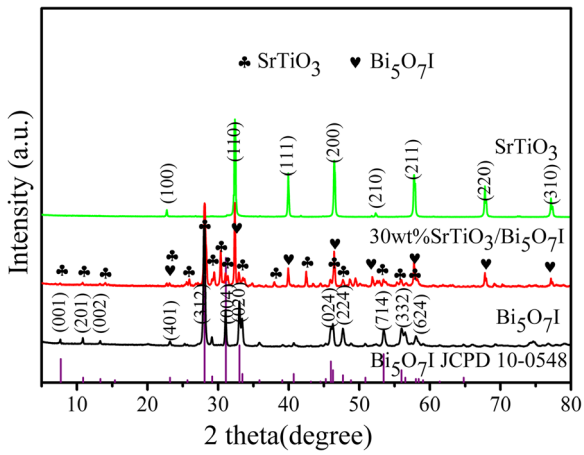


**Fig. 1** XRD patterns of pure $Bi_5O_7I$, $SrTiO_3$ and 30 wt% $SrTiO_3/Bi_5O_7I$ nanocomposite

(401), (312), (004), (020), (024), (224), (714), (332), and (624) planes of the $Bi_5O_7I$ (JCPDS No. 10-0548), respectively [28]. The strongest peak is corresponding to the (312) crystal plane of $Bi_5O_7I$. From the XRD pattern of the 30 wt% $SrTiO_3/Bi_5O_7I$ nanocomposite, it can be found that all prominent diffraction peaks are arising from tetragonal $Bi_5O_7I$ and perovskite $SrTiO_3$. There are no other obvious peaks of impurity observed, which indicates that the $Bi_5O_7I$ and SrTiO3 phases coexist in the composite.

## XPS Analysis

The XPS measurements provide further information for the evaluation of the surface elemental composition and purity of the 30 wt% $SrTiO_3/Bi_5O_7I$ nanocomposite. The binding energy obtained in the XPS analysis was corrected for specimen charging by referencing C 1 s to 284.65 eV, and the results are displayed in Fig. 2. The XPS survey scan spectrum of the composite is shown in Fig. 2a, which reveals the existence of Ti, Sr, Bi, I, and O elements in the composite. The two strong peaks at 159.02 and 164.25 eV are respectively assigned to Bi $4f_{5/2}$ and Bi $4f_{7/2}$ peaks of $Bi^{3+}$ in the $SrTiO_3/Bi_5O_7I$ nanocomposites as shown in Fig. 2b [29]. In the XPS spectra of I 3d shown in Fig. 2c, the two strong peaks at 617.88 and 630.22 eV, corresponding to I $3d_{5/2}$ and I $3d_{3/2}$, respectively, suggest the −1 oxidation state of iodine [30]. As shown in Fig. 2d, the binding energies of Ti $2p_{3/2}$ and Ti $2p_{1/2}$ correspond to the peaks at 457.90 and 463.80 eV in the spectrum of Ti 2p, respectively. The peak separation between the Ti $2p_{3/2}$ and Ti $2p_{1/2}$ is 5.90 eV, which indicates a + 4 oxidation state of Ti in the SrTiO3/$Bi_5O_7I$ composites [31]. In Fig. 2e, the peaks at 132.50 and 134.25 eV correspond to the binding energies of Sr $3d_{5/2}$ and Sr $3d_{3/2}$, respectively, indicating its existence in the $Sr^{2+}$ state [32]. In Fig. 2f, the peaks at 529.65 and 531.25 eV are attributed to O 1 s. The peak at 529.65 eV is ascribed to the lattice oxygen of $SrTiO_3$/

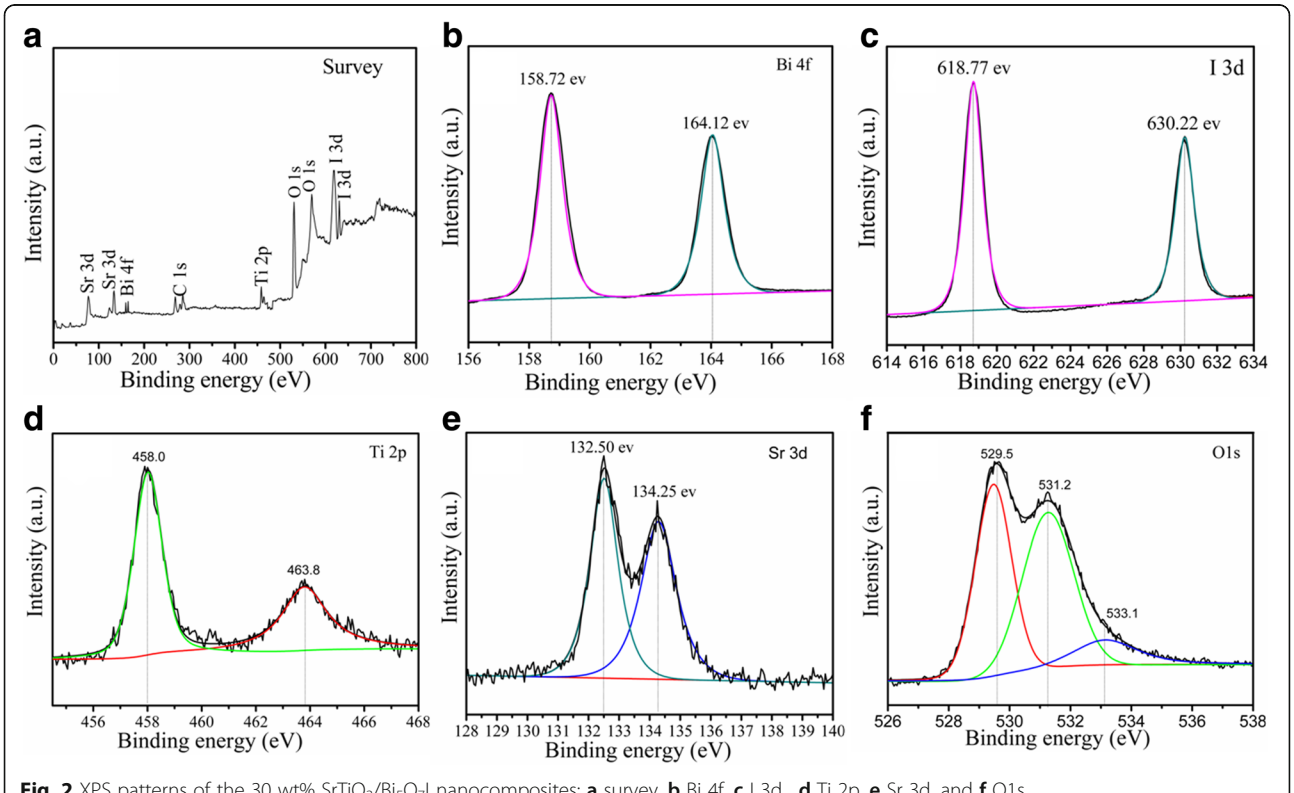


**Fig. 2** XPS patterns of the 30 wt% $SrTiO_3/Bi_5O_7I$ nanocomposites: **a** survey, **b** Bi 4f, **c** I 3d , **d** Ti 2p, **e** Sr 3d, and **f** O1s

$Bi_5O_7I$ nanocomposites, and the peak at 531.25 eV is generally attributed to the chemisorbed oxygen caused by oxygen vacancies [33]. The XPS result further confirms the formation of $SrTiO_3/Bi_5O_7I$ nanocomposites, and intimate integration has been achieved, which agrees well with the XRD results.

## SEM and EDS Analysis

The surface compositions and morphologies of as-prepared pure $SrTiO_3$, $Bi_5O_7I$ and 30 wt% $SrTiO_3/Bi_5O_7I$ nanocomposite were observed by FE-SEM. As seen in Fig. 3a, pure $SrTiO_3$ is composed of spheroidal or spherical particles with diameters in the range of 50~300 nm. The smaller sized $SrTiO_3$ particles are obviously aggregated together to some extent. In Fig. 3b, for the $Bi_5O_7I$ nanosheets, they have an average size about 1 μm and a thickness in the range of 80~100 nm, which is similar to that reported previously [13]. In contrast, after the combination the $Bi_5O_7I$ is not of nanosheets but of nanorods morphology, which is constructed by plenty of nanorods, as shown in Fig. 3c. For the $Bi_5O_7I$ nanorods, the length is in the range of 100~300 nm and the average diameter is about 80 nm. It can be clearly seen that $SrTiO_3$ particles are tightly adhered on the surface of $Bi_5O_7I$ nanorods, and it is thought to be favorable for the photocatalytic performance. Furthermore, EDS was further used to analyze the chemical composition of the 30 wt% $SrTiO_3/Bi_5O_7I$ nanocomposite. As shown in Fig. 3d, the observed C signal can be derived from the conductive adhesive which is used to fix the sample. It is noted that EDS is suitably used for the quantitative determination of the content of heavy elements (e.g., Bi, Ti, I, and Sr), but not for the light elements (e.g., P and O) [34]. The atomic ratio of Bi to I is obtained as 11/63 from the EDS spectrum, which agrees well with the Bi/I atomic ratio of $Bi_5O_7I$ phase. The atomic ratio of Sr/Bi is very close to 1/12.5, implying that $SrTiO_3$ phase accounts for about 30% of the total molar content of the composite.

## Optical Properties Analysis

The UV-vis DRS spectra of the different catalysts are shown in Fig. 4a. The pure $SrTiO_3$ exhibits an absorption band edge at 380 nm in the UV region, which might be attributed to the wide band gap energy [35, 36]. The $Bi_5O_7I$ shows a much longer absorption edge of 520 nm, which can respond to the visible light. The absorption edge of the $SrTiO_3/Bi_5O_7I$ nanocomposites are 480~520 nm. Compared with pure $SrTiO_3$, after coupling with $Bi_5O_7I$ nanosheets, the absorption peak intensity of the $SrTiO_3/Bi_5O_7I$ nanocomposites enhanced significantly.

Based on the absorption spectra, the $E_g$ of the semiconductor can be calculated from the A ν = A ( $\nu - E_g)^{n/2}$ equation [37]. The values of $n$ for $SrTiO_3$ and $Bi_5O_7I$ are 4 and 1, respectively. The band gap energy of the $SrTiO_3$ can be estimated from the plot (A ν)$^2$ versus ploton energy ( ν), and the band gap energy of the $Bi_5O_7I$ can be estimated from the plot (A ν)$^{1/2}$ versus ν. The intercept of the tangent to the $X$ axis gives an approximation of the band gap energy of the samples as displayed in Fig. 4b. The values of band gap energy of pure $Bi_5O_7I$, 30 wt% $SrTiO_3/Bi_5O_7I$ nanocomposite and pure $SrTiO_3$ are about 2.31, 2.38, and 3.2 eV, respectively, which are consistent with the reported values in the relevant literature [38, 39].

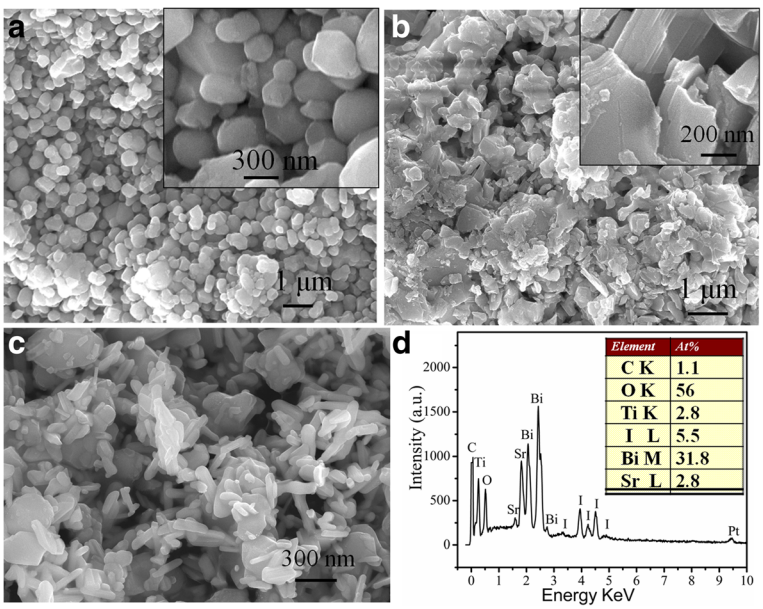


**Fig. 3** SEM images of **a** pure $SrTiO_3$, **b** pure $Bi_5O_7I$, **c** 30 wt% $SrTiO_3/Bi_5O_7I$ nanocomposite, and **d** EDS spectrum of 30 wt% $SrTiO_3/Bi_5O_7I$ nanocomposite

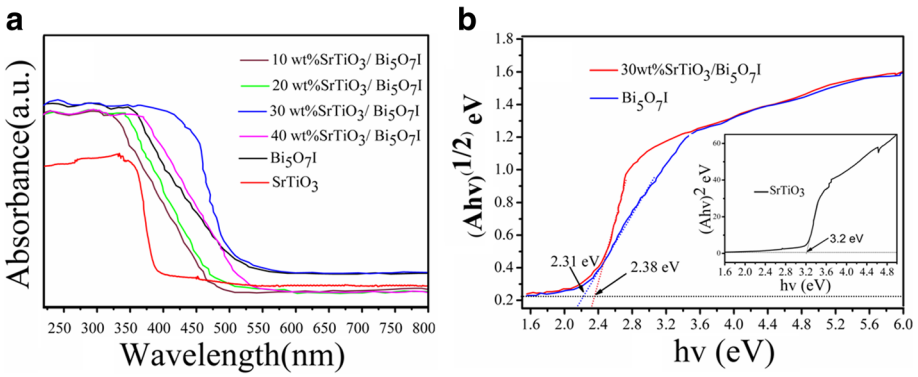


**Fig. 4** **a** DRS spectra of $SrTiO_3/Bi_5O_7I$ nanocomposites and **b** the Tauc plot of $(Ahv)^{1/2}$ versus hv the pure $Bi_5O_7I$ and 30 wt% $SrTiO_3/Bi_5O_7I$ nanocomposite, the Tauc plot of $(Ahv)^2$ versus hv the pure $SrTiO_3$ inset picture of **b**

### FTIR Spectroscopy Analysis

The $Bi_5O_7I$ and $SrTiO_3/Bi_5O_7I$ nanocomposites were further characterized using FTIR spectroscopy to analyze their chemical bonding. As shown in Fig. 5. It can be seen that in almost all samples the adsorption bands of 3445.5 and 1621.9 $cm^{-1}$were due to the O–H stretching vibration and deformation vibration of chemisorbed water molecules [40]. The band at 2906.5 $cm^{-1}$ is ascribed to the Ti–O stretching vibration [41]. The other peaks in the range of 1471.6–500 $cm^{-1}$ correspond to the stretching and deformation modes involving in Bi–O bonds [42].

### Photocatalytic Activity

As $Bi_5O_7I$ and $SrTiO_3$ have very distinct photo absorption and $SrTiO_3$ mainly responds to UV light, simulated solar light and UV light under the same condition are separately employed as the light source to explore the photocatalytic performance of $Bi_5O_7I$, $SrTiO_3$, and $SrTiO_3/Bi_5O_7I$ nanocomposites. Figure 6a displays the degradation curves of RhB under simulated solar light irradiation. It is observed that RhB is stable and hardly decomposed without the catalyst under simulated solar irradiation for 150 min. The pure $SrTiO_3$ shows moderate catalytic activity, and only 18% RhB reduction was achieved after 150 min irradiation. It is attributed to the low light absorption of $SrTiO_3$ in the visible light region or its large band gap energies. Pure $Bi_5O_7I$ displays a very distinct activity which degrades over 52% of RhB in 150 min. Compared with pure $SrTiO_3$ and $Bi_5O_7I$, the $SrTiO_3/Bi_5O_7I$ nanocomposites display a significantly enhanced photocatalytic activity under the same condition. With the increase of $SrTiO_3$ content from 10 to 40%, the photocatalytic activity of the composites increases firstly and then decreases, and the highest photocatalytic activity is observed for the 30 wt% $SrTiO_3/Bi_5O_7I$ nanocomposite. For this optimal composite, the dye degradation reaches approximately 89.6% under simulated solar light irradiation for 150 min. Such a high activity can be ascribed to the photogenerated electrons having a faster mobility and separation.

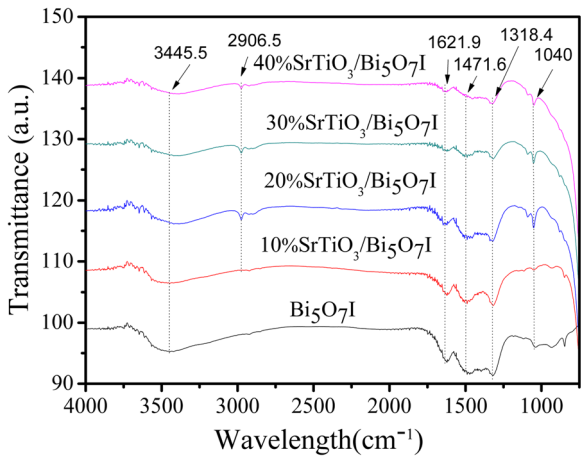


**Fig. 5** FTIR spectra of the pure $Bi_5O_7I$ and $SrTiO_3/Bi_5O_7I$ nanocomposites

To further understand the reaction kinetics of RhB photocatalytic degradation for different photocatalysts, the photocatalytic degradation efficiency were computed using the following equation: $\ln(C_0/C_t) = K_{app}t$, where $C_0$, $C_t$, and $K_{app}$ are representative of the initial concentration, the concentration at time t, and the apparent pseudo-first-order rate constant, respectively [43]. The $-\ln(C_t/C_0)$ exhibits a well linear relationship with irradiation time and the photocatalytic reaction belongs to the pseudo-first-order reaction as shows in Fig. 6b. The $k_{app}$ values obtained for $Bi_5O_7I$, $SrTiO_3$, 10 wt% $SrTiO_3/Bi_5O_7I$, 20 wt% $SrTiO_3/Bi_5O_7I$, 30 wt% $SrTiO_3/Bi_5O_7I$, and 40 wt% $SrTiO_3/Bi_5O_7I$ nanocomposites are 1. $16 \times 10^{-3}$, $4.88 \times 10^{-3}$, $9 \times 10^{-3}$, $1.06 \times 10^{-2}$, $1.45 \times 10^{-2}$, and $9.24 \times 10^{-3}$ $min^{-1}$, respectively. It is conspicuous that the 30 wt% $SrTiO_3/Bi_5O_7I$ nanocomposite manifests the maximum photocatalytic reaction rate constant, which is about 2.97 times higher than that of bare $Bi_5O_7I$, and 12.5 times higher than that of pure $SrTiO_3$.

The RhB degradation curves over all samples under UV light irradiation are further shown in Fig. 6c. It can

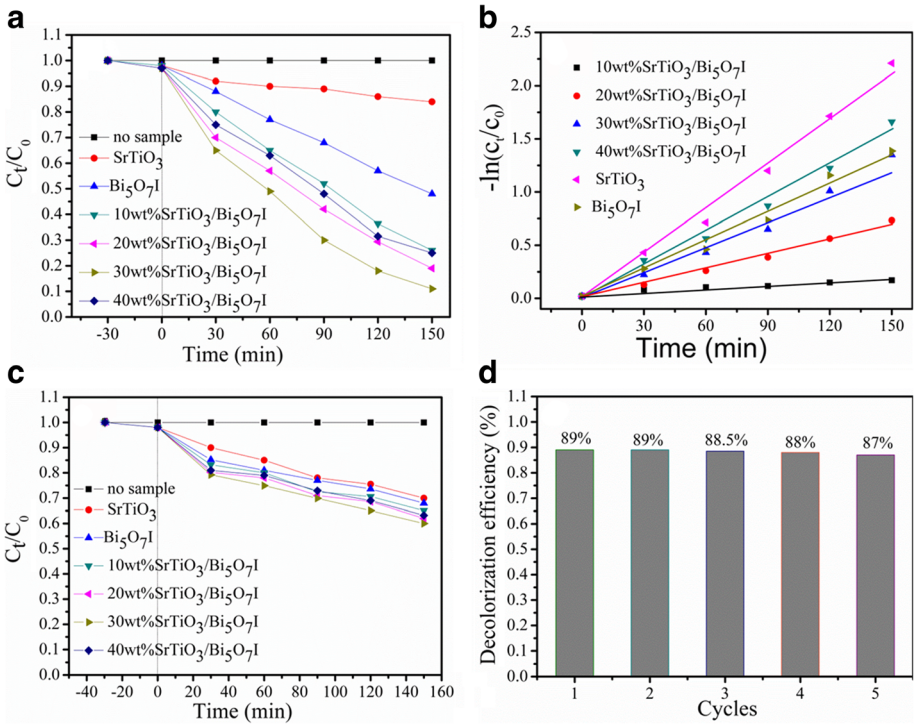


**Fig. 6** **a** Photocatalytic degradation of RhB solution for all samples under simulated solar light irradiation. **b** Plots of $-\ln(C_t/C_0)$ vs time for all samples. **c** Photocatalytic degradation of RhB solution for all samples under UV light illumination. **d** Cycling degradation efficiency of RhB over the $SrTiO_3/Bi_5O_7I$ nanocomposites

be clearly seen that the phenomenon is similar to that in Fig. 6a. However, all samples present a very low photocatalytic efficiency due to the little absorption of UV light, and dye sensitization has an effect on the photocatalytic activity. As shown in Fig. 6a, the 30 wt% $SrTiO_3/Bi_5O_7I$ nanocomposite still displays the best activity; however, the photodegradation of RhB is only 40% within 150 min. These results demonstrate that the $SrTiO_3/Bi_5O_7I$ nanocomposites possess more efficient photocatalytic activity under simulated solar light irradiation.

The stability and reusability of the 30 wt% $SrTiO_3/Bi_5O_7I$ nanocomposite was conducted by repeating the tests for the RhB degradation. After each cycle, the $SrTiO_3/Bi_5O_7I$ nanocomposites were reused in the next cycle before being collected by centrifugation, washed several times with deionized water and ethyl alcohol, and finally dried at 80 °C for 3 h. As shown in Fig. 6d, the photocatalytic activity of the composite does not decrease obviously even after the fifth recycle under simulated solar irradiation, which suggests a good stability for recycling the 30 wt% $SrTiO_3/Bi_5O_7I$ nanocomposite.

## Photocatalytic Mechanism Discussion

In order to gain some insight into the active species involved in the photodegradation of $SrTiO_3/Bi_5O_7I$ nanocomposites, we carried out reactive species trapping experiments over the 30 wt% $SrTiO_3/Bi_5O_7I$ nanocomposite to ascertain the main active species in photocatalytic reaction. As shown in Fig. 7, the addition of the isopropanol (IPA) has almost no effect on the RhB degradation over the $SrTiO_3/Bi_5O_7I$ nanocomposites, which indicates that no •OH radicals are generated. On the contrary, a significant decrease in the dye degradation is observed after the addition of benzoquinone (BQ) or

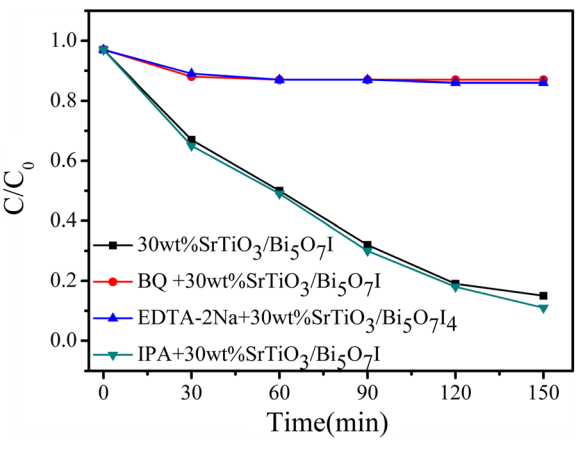


**Fig. 7** The degradation efficiency constant of RhB over the 30 wt% $SrTiO_3/Bi_5O_7I$ nanocomposite in the presence of various scavengers

ethylenediaminetetraacetic acid disodium salt (EDTA-2Na), which implies that $\bullet O_2^-$ and holes are the primary reactive substances for RhB photodegradation.

In order to investigate the charge separation of the as-prepared photocatalysts, the PL spectroscopy was further introduced. Figure 8 shows the comparison of the PL spectra between $Bi_5O_7I$ and 30 wt% $SrTiO_3/Bi_5O_7I$ nanocomposite under the excitation at 320 nm. The PL spectra of both samples are characterized by a peak at 497 nm, which is attributed to the emission of band gap transition energy of $Bi_5O_7I$. However, there is a sharp decrease in the intensity of the 30 wt% $SrTiO_3/Bi_5O_7I$ nanocomposite. This phenomenon demonstrates an efficient separation of the photogenerated carriers within the composite between $SrTiO_3$ and $Bi_5O_7I$.

To better understand the mechanism of the enhanced photocatalytic activity of the $SrTiO_3/Bi_5O_7I$ nanocomposites under simulated solar light irradiation, the corresponding CB and VB positions for $SrTiO_3$ and $Bi_5O_7I$ are theoretically computed according to $E_{VB} = \chi - E_0 + \frac{1}{2}E_g$ and $E_{CB} = E_{VB} - E_g$, where $E_{VB}$ is the VB potential, $E_{CB}$ is the CB potential, $E_0$ is the energy of free electrons on the hydrogen scale (ca. 4.5 eV), $E_g$ is the band gap energy, and $\chi$ is calculated as the geometric mean of the Mulliken electronegativities of the components in the semiconductor [44]. Therefore, the $E_{VB}$ and $E_{CB}$ of $Bi_5O_7I$ were computed to be 2.92 and 0.56 eV, whereas the energies of $SrTiO_3$ were about 2.03 and − 1.15 eV, respectively. These two semiconductors have suitable band potentials and thus can construct a composite structure.

According to the above results, a schematic illustration of energy bands matching between $SrTiO_3$ and $Bi_5O_7I$ and possible ways of charges transfer are depicted in Fig. 9. Both $SrTiO_3$ and $Bi_5O_7I$ are excited under simulated solar light (UV light), and the electrons in the VB of both $SrTiO_3$ and $Bi_5O_7I$ would be excited to the CB, the holes

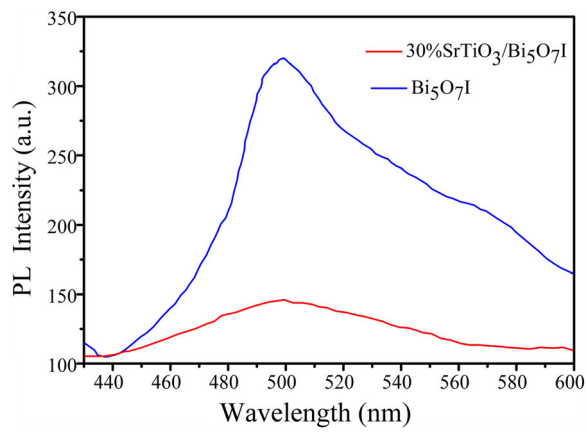


**Fig. 8** PL spectra of pure $Bi_5O_7I$ nanosheets and 30 wt% $SrTiO_3/Bi_5O_7I$ nanocomposite

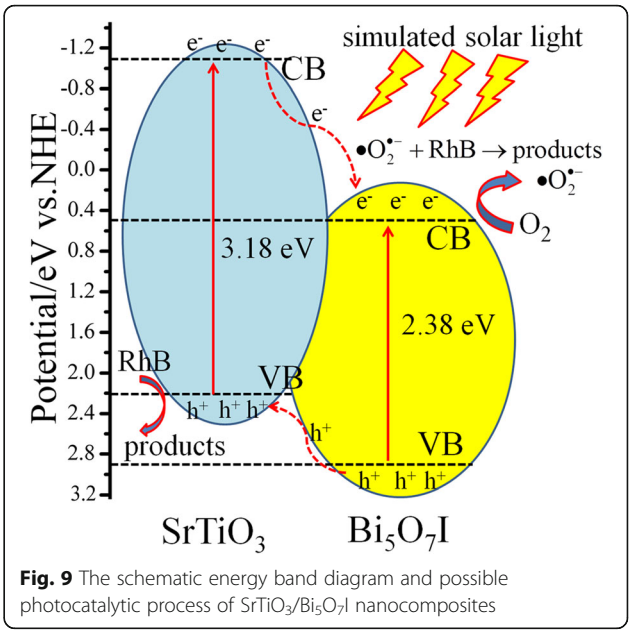


**Fig. 9** The schematic energy band diagram and possible photocatalytic process of $SrTiO_3/Bi_5O_7I$ nanocomposites

remained in its VB. As the CB potential of $SrTiO_3$ (− 1.15 eV) is more negative than that of $Bi_5O_7I$ (+ 0.56 eV), the electrons of $SrTiO_3$ are easily injected into the CB of $Bi_5O_7I$. The photogenerated electrons could react with $O_2$ to produce active oxygen species superoxide radical ($\bullet O_2^-$), which then induces the RhB degradation [45]. On the other hand, the holes in the VB of $Bi_5O_7I$ migrate to the VB of $SrTiO_3$, resulting in an effective separation of the photoinduced electrons and holes. In this way, the photogenerated electrons and holes are separated effectively in the $SrTiO_3/Bi_5O_7I$ nanocomposites. The VB of $SrTiO_3$ is 2.23 eV, lower than the redox potential of $\bullet OH/H_2O$ (+ 2.27 eV). According to the relevant reports [46, 47], the VB of $SrTiO_3$ is insufficient to oxidize $H_2O$ into •OH. It indicates that $\bullet O_2^-$ and holes are the main oxygen active species for $SrTiO_3/Bi_5O_7I$ nanocomposites in the RhB decolorization, under simulated solar light irradiation. Therefore, the synthesized $SrTiO_3/Bi_5O_7I$ nanocomposite photocatalyst exhibits a much higher photocatalytic performance than that of $SrTiO_3$ and $Bi_5O_7I$.

## Conclusions

In summary, novel $SrTiO_3/Bi_5O_7I$ nanocomposites photocatalysts have been designed and fabricated by a solvothermal approach coupled with thermal decomposition. XRD, XPS, and EDS measurements illustrate that the products are indeed $SrTiO_3/Bi_5O_7I$ nanocomposites. UV-vis DRS analysis displays that the $SrTiO_3/Bi_5O_7I$ nanocomposites have a good performance of light absorption. The results of PL spectra show that the recombination of photoinduced electron-hole pairs is obviously inhibited in $SrTiO_3/Bi_5O_7I$ nanocomposites.

The obtained nanocomposites show a good stability and a recycling capacity in the photocatalytic process. The as-synthesized $SrTiO_3/Bi_5O_7I$ photocatalysts exhibit a highly efficient photocatalytic property for the degradation of RhB under simulated solar light irradiation, which is superior to that of $SrTiO_3$ and $Bi_5O_7I$. The outstanding photocatalytic activity of the photocatalysts is ascribed to the efficient separation and migration of photogenerated charge carriers. The $\bullet O_2^-$ and holes are the main oxygen-active species causing the dye degradation. This work could provide insights into the design and development of other excellent photocatalytic materials for environmental and energy applications.

#### Abbreviations

BQ: Benzoquinone; CB: Conduction band; DRS: Diffuse reflectance spectra; EDS: Energy-disperse X-ray spectroscopy; EDTA-2Na: Ethylenediaminetetraacetic acid disodium salt; FE-SEM: Field-emission scanning electron microscope; FTIR: Fourier-transform infrared spectroscopy; IPA: Isopropanol; PL: Photoluminescence; RhB: Rhodamine B; UV-vis: Ultraviolet-visible; VB: Valence band; XPS: X-ray photoelectron spectroscopy; XRD: X-ray diffraction

#### Funding

This work was supported by the National Natural Science Foundation of China (61107055), the Specialized Research Fund for the Doctoral Program of Jiangsu University of Technology (KYY17011), and the Jiangsu Province Key Laboratory of Materials Surface Science and Technology (KFBM20170003).

#### Availability of data and materials

All data are fully available without restriction.

#### Authors' contributions

ZH conceived the idea of experiments. YX carried out the preparation and characterization of the samples. YX, ZH, BT, YL, and JS analyzed and discussed the results of the experiments. YX wrote the manuscript, ZH, YL, and JS amended the manuscript. All authors read and approved the final manuscript.

#### Authors' information

Zuming He is a professor and a Ph. D. degree holder specializing in the investigation of photocatalytic and nanometer materials. Yongmei Xia is an associate professor and a Ph. D. degree holder specializing in the investigation of photocatalytic and optical materials. Bin Tang is a professor and a Ph. D. degree holder specializing in the investigation of optical materials. Ya Liu is a professor and a Ph. D. degree holder specializing in the investigation of optical and nanometer materials. Jiangbin Su is a professor and a Ph. D. degree holder specializing in the nanofabrication and the electron beam-induced nanoinstability and nanoprocessing.

#### Competing interests

The authors declare that they have no competing interests.

## Publisher's Note



#### Author details

[1]Jiangsu Key Laboratory of Advanced Material Design and Additive Manufacturing, School of Materials and Engineering, Jiangsu University of Technology, Changzhou 213001, China. [2]Huaide College, Changzhou University, Jingjiang 214500, China. [3]School of Mathematics&Physics, Changzhou University, Changzhou 213164, China. [4]Jiangsu Key Laboratory of Materials Surface Science and Technology, Changzhou University, Changzhou 213164, China.

Received: 1 March 2018 Accepted: 29 April 2018
Published online: 11 May 2018

#### References

1. Raizada P, Singh P, Kumar A, Pare B, Jonnalagadda SB (2014) Zero valent iron-brick grain nanocomposite for enhanced solar-Fenton removal of malachite green. Sep Purif Technol 133:429–437
2. Ye YC, Yang H, Li RS, Wang XX (2017) Enhanced photocatalytic performance and mechanism of Ag-decorated $LaFeO_3$ nanoparticles. J Sol-Gel Sci Technol 82:509–518
3. Singh P, Priya B, Shandilya P, Raizada P, Singh N, Pare B, Jonnalagadda SB (2016) Photocatalytic mineralization of antibiotics using 60%$WO_3$/BiOCl stacked to graphene sand composite and chitosan. Arab J Chem. https://doi.org/10.1016/j.arabjc.2016.08.005
4. Xia YM, Yu XQ, He ZM, Lu YL, Zhang YF, Sun SP, Zhu SQ, Li XP (2017) Synthesis of novel copper-based oxide nanostructured film on copper via solution-immersion. Ceram Int 43:14499–14503
5. Zheng CX, Yang H, Cui ZM, Zhang HM, Wang XX (2017) A novel $Bi_4Ti_3O_{12}$/$Ag_3PO_4$ heterojunction photocatalyst with enhanced photocatalytic performance. Nanoscale Res Lett 12:608
6. Di LJ, Yang H, Xian T, Chen XJ (2017) Enhanced photocatalytic activity of $NaBH_4$ reduced $BiFeO_3$ nanoparticles for Rhodamine B decolorization. Materials 10:1118
7. He ZM, Xia YM, Tang B, Jiang XX, Su JB (2016) Fabrication and photocatalytic property of ZnO/$Cu_2O$ core-shell nanocomposites. Mater Lett 184:148–151
8. Priya B, Shandilya P, Raizada P, Thakur P, Singh N, Singh P (2016) Photocatalytic mineralization and degradation kinetics of ampicillinand oxytetracycline antibiotics using graphene sand composite and chitosan supported BiOCl. J Mol Catal A Chem 423:400–413
9. Priya B, Raizada P, Singh N, Thakur P, Singh P (2016) Adsorptional photocatalytic mineralization of oxytetracycline and ampicillin antibiotics using $Bi_2O_3$/BiOCl supported on graphene sand composite and chitosan. J Colloid Interface Sci 479:271–283
10. Islam MJ, Reddy DA, Han NS, Choi J, Song JK, Kim TK (2016) An oxygen-vacancy rich 3D novel hierarchical $MoS_2$/BiOI/AgI ternary nanocomposite: enhanced photocatalytic activity through photogenerated electron shuttling in a Z-scheme manner. Phys Chem Chem Phys 18:24984–24993
11. Cui ZM, Yang H, Zhao XX (2018) Enhanced photocatalytic performance of g-$C_3N_4$/$Bi_4Ti_3O_{12}$ heterojunction nanocomposites. Mater Sci Eng B 229:160–172
12. He ZM, Xia YM, Tang B, Su JB (2017) Fabrication and photocatalytic property of magnetic $NiFe_2O_4$/$Cu_2O$ composites. Mater Res Express 4:095501
13. Cao J, Li X, Lin HL, Xu BY, Luo BD, Chen SF (2012) Low temperature synthesis of novel rodlike $Bi_5O_7I$ with visible light photocatalytic performance. Mater Lett 76:181–183
14. Sun SM, Wang WZ, Zhang L, Zhou L, Yin WZ, Shang M (2009) Visible-light-induced efficient contaminant removal by $Bi_5O_7I$. Environ Sci Technol 43:2005–2010
15. Huang HW, Zeng C, Xiao K, Zhang YH (2017) Coupling of solid-solution and heterojunction in a 2D-1D core-shell-like $BiOCl_{0.5}I_{0.5}$/$Bi_5O_7I$ hierarchy for promoting full-spectrum photocatalysis and molecular oxygen activation. J Colloid Interface Sci 504:257–267
16. Zhang L, Wang WZ, Sun SM, Zhang ZJ, Xu JH, Ren J (2012) Photocatalytic activity of $Er^{3+}$, $Yb^{3+}$ doped $Bi_5O_7I$. Catal Commun 26:88–92
17. Liu CY, Huang HW, Du X, Zhang TY, Tian N, Guo XY, Zhang YH (2015) In situ co- crystallization for fabrication of g-$C_3N_4$/$Bi_5O_7I$ heterojunction for enhanced visible-light photocatalysis. J Phys Chem C 119:17156–17165
18. Cheng LJ, Kang Y (2015) $Bi_5O_7I$/$Bi_2O_3$ composite photocatalyst with enhanced visible light photocatalytic activity. Catal Commun 72:16–19
19. Wang SM, Guan Y, Wang LP, Zhao W, He H, Xiao J, Yang SG, Sun C (2015) Fabrication of a novel bifunctional material of BiOI/$Ag_3VO_4$ with high adsorption-photocatalysis for efficient treatment of dye wastewater. Appl Catal B Environ 168-169:448–457
20. Cui M, Yu JX, Lin HJ, Wu Y, Zhao LH, He YM (2016) In-situ preparation of Z-scheme AgI/$Bi_5O_7I$ hybrid and its excellent photocatalytic activity. Appl Surf Sci 387:912–920
21. Jia YH, Shen S, Wang DG, Wang X, Shi JY, Zhang FX, Han HX, Li C (2013) Composite $Sr_2TiO_4$/$SrTiO_3$(La, Cr) heterojunction based photocatalyst for hydrogen production under visible light irradiation. J Mater Chem A 1:7905–7912

22. Shah ZH, Ge YZ, Ye WY, Lin XJ, Zhang SF, Lu RW (2017) Visible light activation of $SrTiO_3$ by loading Ag/AgX (X = Cl, Br) for highly efficient plasmon-enhanced photocatalysis. Mater Chem Phys 198:73–82
23. Guo JJ, Ouyang SX, Li P, Zhang YJ, Kako T, Ye JH (2013) A new heterojunction $Ag_3PO_4$/Cr- $SrTiO_3$ photocatalyst towards efficient elimination of gaseous organic pollutants under visible light irradiation. Appl Catal B Environ 134-135:286–292
24. Chen C, Dai QL, Miao C, Xu L, Song HW (2015) Strontium titanate nanoparticles as the photoanode for CdS quantum dot sensitized solar cells. RSC Adv 5:4844–4852
25. Xia YM, He ZM, Lu YL, Tang B, Sun SP, Su JB, Li XP (2018) Fabrication and photocatalytic property of magnetic $SrTiO_3/NiFe_2O_4$ heterojunction nanocomposites. RSC Adv 8:5441–5450
26. Xia YM, He ZM, Su JB, Tang B, Hu KJ, Lu YL, Sun SP, Li XP (2018) Fabrication of magnetically separable $NiFe_2O_4$/BiOI nanocomposites with enhanced photocatalytic performance under visible-light irradiation. RSC Adv 8:4284–4294
27. Kim CW, Suh SP, Choi MJ, Kang YS, Kang YS (2013) Fabrication of $SrTiO_3$-$TiO_2$ heterojunction photoanode with enlarged pore diameter for dye-sensitized solar cells. J Mater Chem A 1:11820–11827
28. Su YR, Wang H, Ye LQ, Jin XL, Xie HQ, He CZ, Bao KY (2014) Shape-dependent photocatalytic activity of $Bi_5O_7I$ caused by facets synergetic and internal electric field effects. RSC Adv 4:65056–65064
29. Mousavi M, Yangjeh AH (2016) Magnetically separable ternary g-$C_3N_4$/$Fe_3O_4$/BiOI nanocomposite novel visible-light-driven photocatalysts based on graphitic carbon nitride. J Colloid Interface Sci 465:83–92
30. Yuan D, Huang LY, Li YP, Xu YG, Xu H, Huang SQ, Yan J, He MQ, Li HM (2016) Synthesis and photocatalytic activity of g-$C_3N_4$/BiOI/BiOBr ternary composites. RSC Adv 6:41204–41203
31. Zhao X, Yang H, Cui Z, Li R, Feng W (2017) Enhanced photocatalytic performance of Ag-$Bi_4Ti_3O_{12}$ nanocomposites prepared by a photocatalytic reduction method. Mater Technol 32:870–880
32. Zhou J, Yin L, Zha K, Li HR, Liu ZY, Wang JX, Duan K, Feng B (2016) Hierarchical fabrication of heterojunctioned $SrTiO_3/TiO_2$ nanotubeson 3D microporous Ti substrate with enhanced photocatalytic activity and adhesive strength. Appl Surf Sci 367:118–125
33. Wang F, Yang H, Zhang YC (2018) Enhanced photocatalytic performance of $CuBi_2O_4$ particles decorated with Ag nanowires. Mater Sci Semicond Process 73:58–66
34. Wang F, Yang H, Zhang HM, Jiang JL (2018) Growth process and enhanced photocatalytic performance of $CuBi_2O_4$ hierarchical microcuboids decorated with AuAg alloy nanoparticles. J Mater Sci Mater Electron 29:1304–1316
35. Ruzimuradov O, Hojamberdiev M, Fasel C, Riedel R (2017) Fabrication of lanthanum and nitrogen-co-doped $SrTiO_3$-$TiO_2$ heterostructured macroporous monolithic materials for photocatalytic degradation of organic dyes under visible light. J Alloys Compd 699:144–150
36. Wang L, Wang ZJ, Wang DH, Shi XC, Song H, Gao XQ (2014) The photocatalysis and mechanism of new $SrTiO_3/TiO_2$. Solid State Sci 31:85–90
37. Xia YM, He ZM, Yang W, Tang B, Lu YL, Hu KJ, Su JB, Li XP (2018) Effective charge separation in BiOI/$Cu_2O$ composites with enhanced photocatalytic activity. Mater Res Express 5:025504
38. Yang J, Xu LJ, Liu CL, Xie TP (2014) Preparation and photocatalytic activity of porous $Bi_5O_7I$ nanosheets. Appl Surf Sci 319:265–271
39. Ding CH, Ye LQ, Zhao Q, Zhong ZG, Liu KC, Xie HQ, Bao KQ, Zhang XG, Huang ZX (2016) Synthesis of $Bi_xO_yI_z$ from molecular precursor and selective photoreduction of $CO_2$ into CO. J CO2 Util 14:135–142
40. Chou SY, Chen CC, Dai YM, Lin JH, Lee WW (2016) Novel synthesis of bismuth oxyiodide/graphitic carbon nitride nanocomposites with enhanced visible-light photocatalytic activity. RSC Adv 6:33478–33491
41. Yang SF, Niu CG, Huang DW, Zhang H, Liang C, Zeng GM (2017) $SrTiO_3$ nanocubes decorated with Ag/AgCl nanoparticles as photocatalysts with enhanced visible-light photocatalytic activity towards the degradation of dyes, phenol and bisphenol A. Environ Sci Nano 4:585–595
42. Chen DM, Hao QA, Wang ZH, Ding H, Zhu YF (2016) Influence of phase structure and morphology on the photocatalytic activity of bismuth molybdates. CrystEngComm 18:1976–1986
43. Zhou M, Yang H, Xian T, Li RS, Zhang HM, Wang XX (2015) Sonocatalytic degradation of RhB over $LuFeO_3$ particles under ultrasonic irradiation. J Hazard Mater 289:149–157
44. Zhao Q, Liu X, Xing Y, Liu Z, Du C (2017) Synthesizing $Bi_2O_3$/BiOCl heterojunctions by partial conversion of BiOCl. J Mater Sci 52:2117–2130
45. Yu YG, Chen G, Wang X, Jia DC, Tang PX, Lv CD (2015) A facile approach to construct BiOI/$Bi_5O_7I$ composites with heterostructures: efficient charge separation and enhanced photocatalytic activity. RSC Adv 5:74174–74179
46. Chen HF, Huang BB, Dai Y, Qin XY (2010) Visible-light-induced activity of AgI-BiOI composites for removal of organic contaminants from water and wastewater. Langmuir 26:6618–6624
47. Hahn NT, Hoang S (2012) Spray pyrolysis deposition and photoelectron chemical properties of n-type BiOI nanoplatelet thin films. ACS Nano 6: 7712–7722